第 44 卷 第 7 期/2024 年 4 月/光学学报 研究论文

光学学报

小角X射线散射中宇宙线噪声去除方法

赵晋[1,3]，王成龙[2*]，喻虹[1,2,3]

[1]中国科学院上海光学精密机械研究所量子光学重点实验室，上海 201800；

[2]张江实验室，上海 201210；

[3]中国科学院大学，北京 100049

摘要 针对小角X射线散射(SAXS)测量图样中的宇宙线提出一种去除方法，以纳米结构的周期信息为物理先验计算得到周期性散射信号的坐标信息，对各光斑级次有效信号区域内的宇宙线进行检测并去除。数值模拟了含宇宙线的SAXS测量图样序列，测试该方法对SAXS测量图样序列宇宙线的检测和去除效果，并与现有的宇宙线去除方法进行对比。计算不同曝光时间下去噪前和各方法去噪后SAXS测量图样的评价指标，可以说明该方法对于SAXS测量图样中的宇宙线具有良好的去除效果，并能在长曝光条件下获得明显的信噪比增益。

关键词 X射线光学；小角X射线散射；周期性纳米结构；宇宙线；去噪

中图分类号 O434.19 **文献标志码** A **DOI**：10.3788/AOS231923

1 引 言

1895年X射线被伦琴发现[1]，从而发展了众多基于X射线的测量物质成分和结构的实验方法[2-9]，小角X射线散射(SAXS)就是其中一种纳米尺度范围内探测物质结构信息的有力工具。20世纪30年代到50年代，Guinier等[10]、Debye等[11]、Porod等[12]和Hosemann等[13]逐步建立并完善了SAXS的理论，随后并将SAXS广泛应用于生物大分子、高聚物材料等众多领域[14-17]。21世纪以来，SAXS被用来表征集成电路(IC)中周期性纳米结构的关键尺寸(CD)、侧壁角(SWA)等三维结构信息[18-19]。SAXS测量凭借其测量精度高和穿透性强等特点能更好地满足目前IC在线测量的需求[20-21]，具有重要的实际应用的价值。

面向IC在线测量的SAXS通常基于小型X射线源[20]。由于小型X射线源的光源亮度有限，基于小型X射线源的SAXS测量需要通过增长曝光时间来提高SAXS信号的信噪比[22]。在长曝光时间的积累下，可以在SAXS测量图样中观察到大量的宇宙线[20,22]。宇宙线是来自宇宙的高能粒子流[23]，撞击到探测器上会产生明显的径迹。作为一种与信号非相关的噪声，宇宙线会随机地出现在散射图样的任意位置从而造成信号失真，严重影响到纳米结构信息的提取。现有的关于宇宙线去除的研究工作主要面向天文观测领域：Shaw等[24]提出了多帧中值像素拒绝算法，van Dokkum[25]提出了基于Laplacian边缘检测的宇宙线去除算法，Shamir[26]提出了基于人眼感知能力的宇宙线去除算法。根据SAXS的基本原理，周期性纳米结构SAXS测量图样的散射信号具有明显的周期分布特点。现有的宇宙线去除方法缺少对上述物理先验信息的充分考虑，对全局图样进行无差别处理，因此无法甄别和去除测量图样中对散射信号存在实质影响的宇宙线分量，难以保证SAXS信号的探测信噪比。

本文提出了一种去除周期性纳米结构SAXS测量图样中宇宙线噪声的方法，以周期性纳米结构的二维周期分布信息为物理先验，计算得到周期性散射信号的坐标信息，针对各散射级次有效信号区域内的宇宙线进行识别并去除。数值模拟了带有宇宙线的SAXS测量图样序列，测试了该方法对图样序列宇宙线的检测和去除效果，并与Laplacian边缘检测算法和多帧中值像素拒绝算法进行了对比，同时分析了不同曝光时间下各方法的宇宙线去除性能，证明了该方法对SAXS测量图样有效信号区域的宇宙线噪声具备良好的去除效果。

2 基本理论

2.1 SAXS测量原理

SAXS测量的原理如图1所示，X射线源发出的X射线聚焦准直后入射到二维周期性的纳米结构样品

收稿日期：2023-12-12；**修回日期**：2024-01-05；**录用日期**：2024-01-10；**网络首发日期**：2024-02-20

基金项目：项目受张江实验室支持

通信作者：*wangcl@zjlab.ac.cn

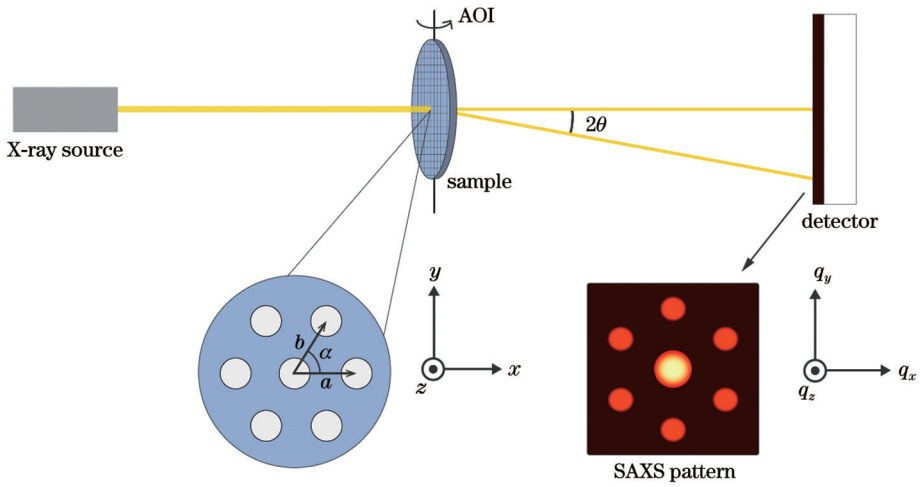

图 1　小角 X 射线散射测量原理图

Fig. 1　Schematic diagram of small-angle X-ray scattering measurement

上，再经样品散射到二维像素探测器上形成散射图样，此时散射角很小，为 2θ。其中，q_x、q_y、q_z 分别为倒易空间矢量 $\boldsymbol{q}$ 在 x、y、z 方向上的分量，α 为两周期方向的夹角，a 为 x 方向上的单位周期间隔，b 为与 x 轴成 α 角方向上的单位周期间隔。入射 X 射线相对于样品二维周期平面的法线的夹角为入射角（AOI），通过旋转样品得到 AOI 不同的散射图样，实现对样品三维结构的测量。

由于原子对 X 射线的二次散射强度极低，可忽略不计，因此在一阶玻恩近似（Born approximation）中的散射复振幅可由样品电子密度的傅里叶变换[27]得到，该过程具体表达式为

$$A(\boldsymbol{q})=\mathrm{F}\{\rho(\boldsymbol{r})\}=\int\rho(\boldsymbol{r})\exp(-\mathrm{i}\boldsymbol{q}\cdot\boldsymbol{r})\mathrm{d}\boldsymbol{q},\tag{1}$$

式中：$\mathrm{F}\{\cdot\}$ 为傅里叶变换运算；$\boldsymbol{r}$ 为实空间位置矢量；$\rho(\boldsymbol{r})$ 为样品的电子密度；$A(\boldsymbol{q})$ 为散射复振幅。那么探测面上散射强度 $I(\boldsymbol{q})$[27] 的表达式为

$$I(\boldsymbol{q})=I_0\left|A(\boldsymbol{q})\right|^2=I_0\left|F(\boldsymbol{q})S(\boldsymbol{q})\right|^2,\tag{2}$$

式中：I_0 为入射 X 射线强度；$F(\boldsymbol{q})$ 为形状因子；$S(\boldsymbol{q})$ 为结构因子。SAXS 强度 $I(\boldsymbol{q})$ 为倒易空间矢量 $\boldsymbol{q}$ 的函数，$\boldsymbol{q}$ 又称散射矢量，是散射波与入射波的矢量差，这说明探测面上不同 $\boldsymbol{q}$ 的散射强度对应不同方向的散射波。

对于二维周期性的纳米结构样品，其结构因子 $S(\boldsymbol{q})$[28] 可表示为

$$S(q_x,q_y)=\frac{\sin\left(N_xq_xa/2\right)}{\sin\left(q_xa/2\right)}\frac{\sin\left[N_y\left(q_x\cos\alpha+q_y\sin\alpha\right)b/2\right]}{\sin\left[\left(q_x\cos\alpha+q_y\sin\alpha\right)b/2\right]},\tag{3}$$

式中：N_x 和 N_y 分别为 x 方向和 y 方向上的周期单元数目。当 N_x 和 N_y 足够大时，式（3）化为

$$S(q_x,q_y)=\sum_{M=0}^{N_x-1}\sum_{N=0}^{N_y-1}\delta\left(q_x-2\pi\frac{M}{a}\right)\times\delta\left[q_y-2\pi\left(\frac{N}{b\sin\alpha}-\frac{M}{a\tan\alpha}\right)\right],\tag{4}$$

式中：δ 为狄拉克函数；(M,N) 为周期性散射信号的级次。在倒易空间中，有且仅有 (q_x,q_y) 处有散射信号，该位置满足条件

$$\begin{cases}q_x=2\pi M/a\\ q_y=2\pi\left(\dfrac{N}{b\sin\alpha}-\dfrac{M}{a\tan\alpha}\right)\end{cases}。\tag{5}$$

在实际应用中，由于受到光源发散角和样品尺寸等因素的影响，在散射图样中会出现以各散射信号位置 (q_x,q_y) 为中心的具有一定宽度的 Bragg 峰[29]。因此，周期性纳米结构 SAXS 测量图样的信号是具有周期性和定域性的光斑，散射图样中仅有部分特定的光斑（Bragg 峰）区域对提取纳米结构信息有贡献。将周期性纳米结构样品的二维周期信息 $\{a,b,\alpha\}$ 作为物理先验，将设定的级次代入式（5）即可得到散射图样中信号光斑的中心坐标 (q_x,q_y)，即可识别和去除存在于各级次光斑及其邻域的有效信号区域内的宇宙线噪声。

2.2　SAXS 测量图样宇宙线去除方法

得益于单光子计数型像素探测器的高采样率和无读出噪声及暗电流的特点[30]，叠加多帧短曝光散射图样可得到等效长曝光散射图样[22]。在相同条件下对样品进行多次短曝光，以样品的周期信息为物理先验并计算出信号光斑的中心位置，对图样中的有效信号区域内的宇宙线进行检测，在除去检出受宇宙线实质影响的异常帧图样后，叠加剩余帧从而得到去除宇宙线的 SAXS 测量图样。该方法的处理流程如图 2 所示，具体流程为：

1）在相同条件下对周期性纳米结构样品进行 K 次短曝光，获得包含 K 幅 SAXS 测量图样的序列。

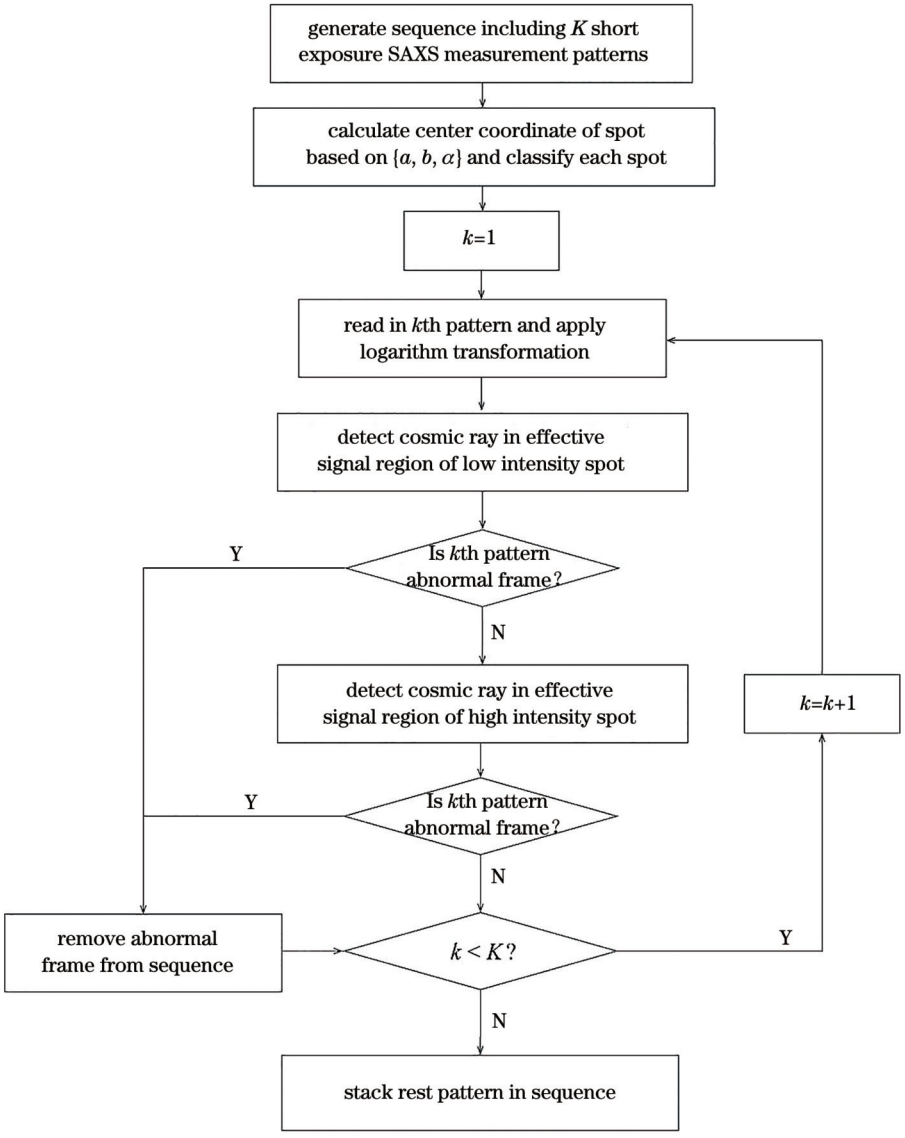

图 2　SAXS 测量图样中宇宙线去除方法流程示意图

Fig. 2　Schematic diagram of process for removing cosmic ray in SAXS measurement pattern

2）设定光斑级次列表$\left\{(M,N)_i\right\}$，由式(5)计算各级次光斑中心位置坐标列表$\left\{\left(q_x,q_y\right)_i\right\}$。从 SAXS 散射图样序列中取单幅图样作对数变换，设定相对应的级次光斑的半径列表$\{r_i\}$，根据各级次光斑信号的占空比将全部级次光斑分为高通量光斑与低通量光斑两类。

对于某一光斑级次，以光斑中心位置$\left(q_x,q_y\right)$为中心、r为半径的圆形区域为光斑掩模，对应该级次光斑的信号占空比R_{D}定义为

$$R_{\mathrm{D}}=N_{\mathrm{s}}/N_{\mathrm{r}},\tag{6}$$

式中：N_{r}为光斑掩模所含全部像素数；N_{s}为光斑掩模内非零像素数。

3）读取图样序列中第k幅图样作对数变换。

4）对于各低通量光斑，在其光斑内及邻域中，对全部连通区域进行遍历。根据连通区域的像素数与连通区域的周方面积比，判定各连通区域是否属于宇宙线。若某一连通区域的判定结果为是，则认为当前帧为异常帧，将其从散射图样序列中移除。

对于某一低通量光斑级次，以光斑中心位置$\left(q_x,q_y\right)$为圆心、$c_{\mathrm{l}}\cdot r$为半径的圆形区域为光斑及邻域掩模，c_{l}为倍率系数。光斑及邻域掩模内某一连通区域的周方面积比R_{PA}定义为

$$R_{\mathrm{PA}}=P_{\mathrm{r}}^2/S_{\mathrm{r}},\tag{7}$$

式中：P_{r}为该连通区域的周长（单位为 pixel）；S_{r}为该连通区域的面积（单位为 pixel）。

5）对于各高通量光斑，在其光斑内及邻域中，对全部连通区域进行遍历，根据连通区域的像素数与连通区域到光斑中心的距离，判定各连通区域是否属于宇宙线。若某一连通区域的判定结果为是，则认为当前帧为异常帧，将其从散射图样序列中移除。

对于某一高通量光斑级次，以光斑中心位置

(q_x, q_y)为中心、r为内径以及$c_h \cdot r$为外径的环形区域为光斑的邻域掩模，其中c_h为倍率系数。

6）令$k=k+1$，重复步骤3）～6）直到全部K幅图样完成检测。叠加图样序列中的剩余图样即为去除宇宙线噪声的SAXS图样。

3　数值仿真与结果分析

数值模拟了SAXS测量周期性纳米结构样品，模拟入射X射线的波长为1.54 Å（1 Å=1×10^{-10} m），待测样品是周期性硅纳米孔结构，由直径为105 nm、深度为3 μm的二维六角格子[31]排布而成，其周期参数$a=b=120$ nm，两周期方向的夹角$\alpha=60°$，样品表面的法线平行于X射线的入射方向。基于2.1节中SAXS测量的基本原理，仿真得到不含任何噪声的理想SAXS测量图样。在此基础上根据曝光时间的长短，对测量图样添加散粒噪声，并从宇宙线公共库[32]中选取不同形状、不同数目的宇宙线噪声单元，随机添加到散射图样中。按照此法重复生成含500幅仿真短曝光SAXS测量图样的序列用于测试所提方法的去噪效果，其中有135幅图样中的宇宙线存在于光斑的有效信号区域内，对散射信号产生了实质影响。

图3（a）与图3（b）分别展示了仿真得到的长曝光与短曝光SAXS测量图样。在长曝光SAXS测量图样中存在大量的宇宙线噪声；而短曝光SAXS测量图样中的宇宙线很少，且十分明显，易于识别和检测。对图3（a）中所有信号光斑按2.1节中所定义的光斑级次(M, N)进行标定，结果如图3（c）所示。由图3（c）中所标定的级次得到光斑级次列表，从而得到2.2节中宇宙线检测所需的掩模，如图3（d）所示。将图3（d）中全部的环形掩模替换为半径与各环形掩模外径相同的圆形掩模，得到感兴趣区域（ROI）掩膜。利用所提方法去除图3（a）中的宇宙线，得到ROI掩模下去除宇宙线后的SAXS图样，如图3（e）所示。对于高级次的低通量光斑，可直接检测和去除光斑内及其邻域中的宇宙线，而低级次的高通量光斑信号较强，难以在光斑内部直接对宇宙线进行检测，故仅对光斑邻域内的宇宙线进行检测和去除。通过将不同通量光斑划分为不同类型的有效信号区域，所提方法可有效去除SAXS测量图样中有效信号区域内的宇宙线。

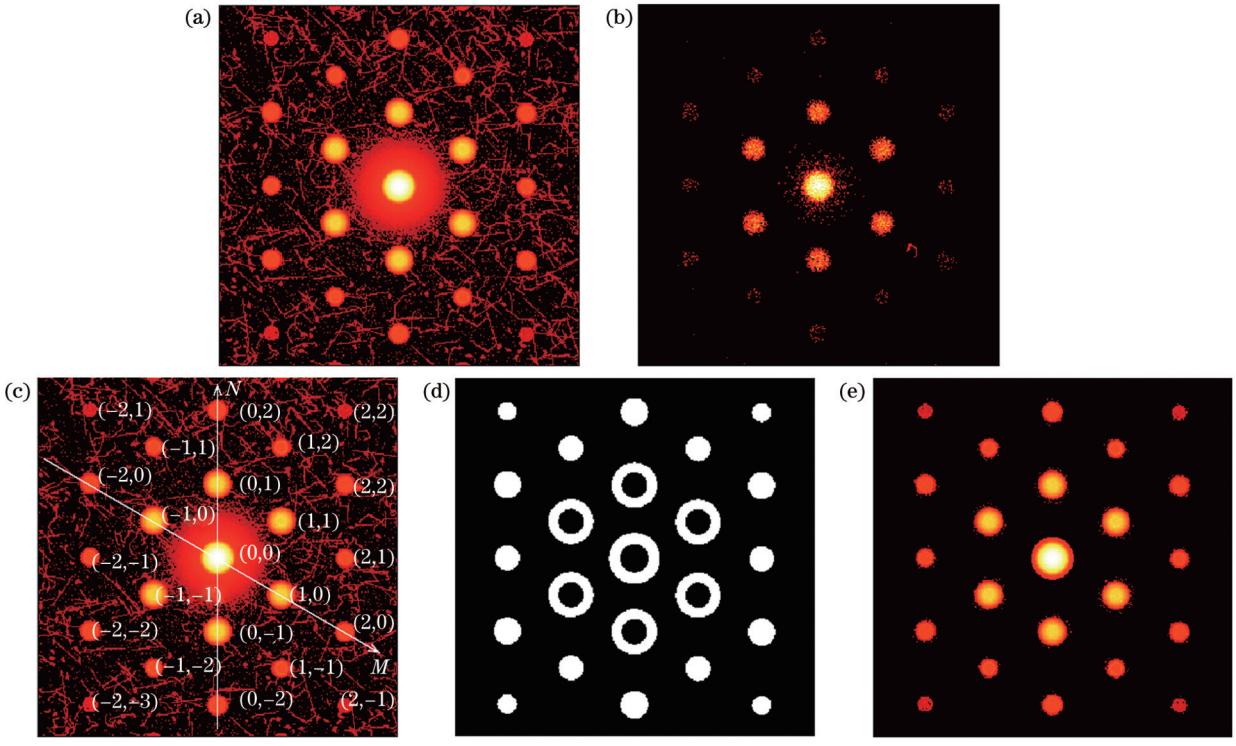

图3　SAXS测量周期性纳米结构的数值仿真结果。（a）仿真长曝光SAXS测量图样；（b）仿真短曝光SAXS测量图样；（c）对长曝光仿真SAXS测量图样中各光斑标定级次；（d）用所提方法去除宇宙线所需的掩模；（e）在ROI掩模下用所提方法去除宇宙线后的仿真长曝光SAXS测量图样

Fig. 3　Numerical simulation results of SAXS measuring periodic nanostructure. (a) Simulated long exposure SAXS measuring pattern; (b) simulated short exposure SAXS measuring pattern; (c) calibrate level of each spot in simulated long exposure SAXS measurement pattern; (d) mask for cosmic ray rejection by proposed method; (e) simulated long exposure SAXS measuring pattern after cosmic ray rejection by proposed method with ROI mask

3.1　宇宙线检测和去除效果

由于单帧图样的宇宙线检测结果会直接影响所提方法的去噪效果，利用该方法对仿真产生的500幅SAXS测量图样序列进行了逐帧检测，并定量评估了

其检测宇宙线噪声的效果。将每帧噪声检测后的异常帧判定看作二分类问题，计算得到检测结果的混淆矩阵[33]如图4所示。可根据混淆矩阵进一步计算检测结果的准确率P、漏检率R_{M}及虚警率R_{FA}[33]，具体表达式为

$$\begin{cases} P=\dfrac{T_{\mathrm{P}}}{T_{\mathrm{P}}+F_{\mathrm{P}}} \\ R_{\mathrm{M}}=\dfrac{F_{\mathrm{P}}}{F_{\mathrm{P}}+T_{\mathrm{N}}} \\ R_{\mathrm{FA}}=\dfrac{F_{\mathrm{N}}}{F_{\mathrm{N}}+T_{\mathrm{P}}} \end{cases}, \tag{8}$$

式中：T_{P}为检出的真实异常帧数；F_{N}为漏检的真实异常帧数；T_{N}为检出的真实正常帧数；F_{P}为误检的错误异常帧数。结果表明，检测出的146帧图样中有128帧为真实异常帧，准确率达到了87.67%；漏检帧为18帧，误检帧为7帧，漏检率和误检率分别仅为4.93%和5.18%。说明该方法对单帧散射图样中的宇宙线具有良好的甄别和检测效果。

		actual class	
		positive 135	negative 365
detected class	positive 146	true positive (T_{P}) 128	false positive (F_{P}) 18
	negative 354	false negative (F_{N}) 7	true negative (T_{N}) 347

图4　所提方法检测结果的混淆矩阵

Fig. 4　Confusion matrix of detection results of proposed method

为进一步定量评估所提方法的宇宙线噪声去除效果，将均方误差E_{MS}、峰值信噪比R_{PSN}和结构相似性S_{S}[34]作为宇宙线去除效果的评价指标，具体表达式为

$$\begin{cases} E_{\mathrm{MS}}(X,Y)=\dfrac{1}{UV}\displaystyle\sum_{i=1}^{U}\sum_{j=1}^{V}\left(X_{ij}-Y_{ij}\right)^2 \\ R_{\mathrm{PSN}}(X,Y)=10\lg\dfrac{V_{\mathrm{MAX}}^2}{E_{\mathrm{MS}}(X,Y)} \\ S_{\mathrm{S}}(X,Y)=\dfrac{\left(2\mu_X\mu_Y+C_1\right)\left(2\sigma_{XY}+C_2\right)}{\left(\mu_X^2+\mu_Y^2+C_1\right)\left(\sigma_X^2+\sigma_Y^2+C_2\right)} \end{cases}, \tag{9}$$

式中：X为待评价图像；Y为理想的参考图像；U和V分别为图像的长和宽；V_{MAX}为图像的像素最大值；μ_X为X的期望；μ_Y为Y的期望；σ_X为X的标准差；σ_Y为Y的标准差；σ_{XY}为X和Y的协方差；C_1和C_2分别为维持稳定的常数。

考虑到SAXS散射图样中仅有部分的有效信号区域对提取结构信息有贡献，因此在宇宙线去除的效果评价中同样仅关注散射图样中的ROI，即在ROI掩膜下进行三种指标的计算评估。选取了Laplacian边缘检测算法和多帧中值像素拒绝算法这两种典型的宇宙线去除方法，对比其去噪效果，得到去噪前和三种宇宙线去除方法去噪后的散射图样，如图5所示。从图5可

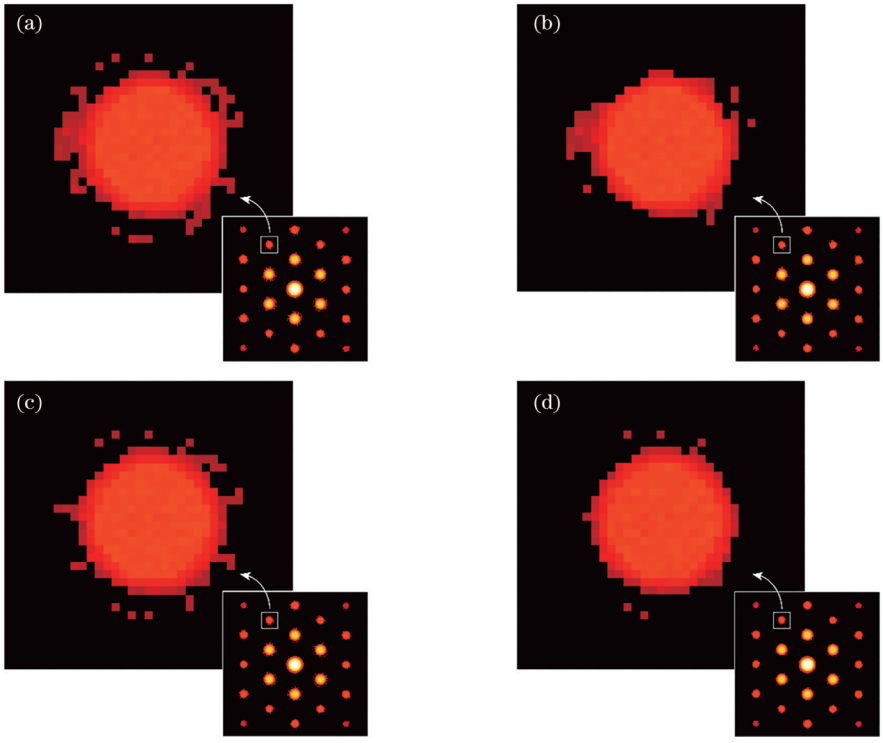

图5　ROI掩模下去噪前和分别用三种方法去噪后SAXS测量图样。(a)去噪前；(b)Laplacian边缘检测去噪；(c)多帧中值像素拒绝去噪；(d)所提方法去噪

Fig. 5　SAXS measuring patterns before and after denoising by three methods respectively under ROI mask. (a) Before denosing; (b) denoised by Laplacian edge detection; (c) denoised by multi-frame median pixel rejection; (d) denoised by proposed method

以看出去噪前散射图样[图 5(a)]的光斑信号及其周围区域内存在明显的宇宙线噪声；Laplacian边缘检测算法去噪后散射图样[图 5(b)]的光斑信号及其周围区域内存在大部分的宇宙线噪声和极少的散粒噪声；多帧中值像素拒绝算法去噪后散射图样[图 5(c)]的光斑信号及其周围区域内存有少部分的宇宙线噪声和散粒噪声；而所提方法去噪得到的散射图样[图 5(d)]获得了最好的去除效果。计算得到去噪前和分别用三种方法去噪后图样的均方误差、峰值信噪比、结构相似性，如表 1 所示。Laplacian边缘检测法和多帧中值像素拒绝法的峰值信噪比增益分别为 −0.67 dB与 2.74 dB，Laplacian边缘检测算法对于SAXS测量图样中的宇宙线噪声几乎没有实质的去除效果，多帧中值像素拒绝算法的去噪效果也不够理想。所提方法的均方误差、峰值信噪比和结构相似性均为最优，去噪后散射图样的峰值信噪比去噪前明显提高了 5.55 dB。充分说明所提方法对宇宙线噪声的去除效果最佳。

表 1 去噪前和分别用三种方法去噪后图样的评价指标

Table 1 Evaluation indexes of denoised patterns before and after denoising by three methods respectively

Index	E_{MS}	R_{PSN} /dB	S_S /%
Before denoising	5.49×10^{-4}	32.60	97.62
Denoised by Laplacian edge detection	6.41×10^{-4}	31.93	97.08
Denoised by multi-frame median pixel rejection	2.92×10^{-4}	35.34	98.59
Denoised by proposed method	1.53×10^{-4}	38.15	99.34

3.2 不同曝光时间下宇宙线去除性能

SAXS测量图样中同时还存在着显著的散粒噪声。在不同的曝光时间下，即不同的叠加帧数下，宇宙线噪声和散粒噪声对SAXS测量图样的影响程度是不同的。在不同曝光时间下的噪声竞争关系也不同，为进一步研究不同噪声竞争关系下所提方法的宇宙线去除性能，从 500 帧的仿真SAXS测量图样序列中随机提取图样，生成新的帧数不同的测量图样序列。分别利用所提方法、Laplacian边缘检测算法和多帧中值像素拒绝算法对新生成的图样序列进行宇宙线噪声的去除，并计算去噪前和利用三种方法去噪后图样的峰值信噪比 R_{PSN} 和对应序列帧数 F_S 的关系，结果如图 6 所示。

测试结果表明，当序列帧数少于 150 时，所提方法

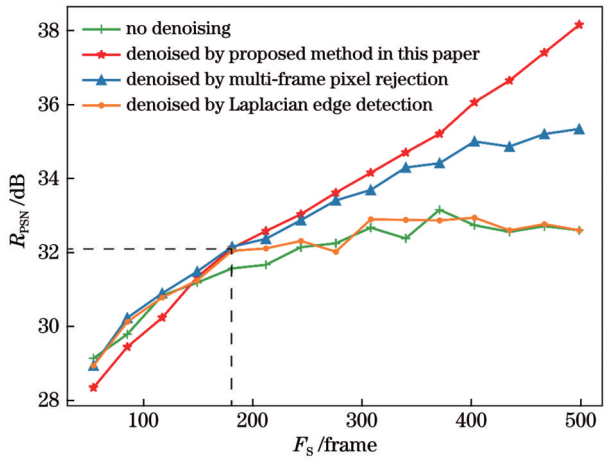

图 6 去噪前和分别用三种方法去噪后图样的 R_{PSN} 和 F_S 的关系

Fig. 6 Relationship between R_{PSN} and F_S of patterns before and after denoising by three methods respectively

得到的去噪图样的峰值信噪比低于去噪前和另外两种对比方法去噪后的图样。此时SAXS测量图样中的散粒噪声占主导地位，测量图样总体的信噪比较低，仍需引入更多的曝光时间(序列帧数)。而当序列帧数超过 180 时，所提方法得到去噪图样的峰值信噪比高于去噪前和另外两种对比方法去噪后的图样，叠加图样的峰值信噪比的水平为 32 dB 左右。此时SAXS测量图样中的散粒噪声的影响减弱，宇宙线噪声的影响逐渐显著，如果不对宇宙线噪声进行去除，将限制峰值信噪比进一步增大。特别地，当序列帧数超过 200 时，去噪前的对照组以及经 Laplacian 边缘检测算法去噪后图样的峰值信噪比不再有明显的区别，因此宇宙线噪声的存在严重限制着探测信号的信噪比上限；而所提方法和多帧中值像素拒绝算法去噪后图样的峰值信噪比仍然能够随序列帧数的增加而提高，并且所提方法峰值信噪比的增速明显高于多帧中值像素拒绝算法。因此，所提方法能够满足SAXS测量图样中去除宇宙线的需求，并且能够在长曝光积累下带来明显的信噪比增益。

4 结 论

提出了一种基于周期性纳米结构的SAXS测量图样中宇宙线噪声去除方法，以纳米结构的二维周期信息为物理先验，计算得到周期性散射信号的坐标信息，对实际影响图样中散射信号的宇宙线分量进行针对性的检测和去除。对周期性纳米结构样品的SAXS测量图样进行了数值仿真，并测试了所提方法对宇宙线的去除效果。测试结果表明，所提方法对单帧散射图样中的宇宙线具有良好的检测效果，去噪后的图样序列比去噪前图样峰值信噪提升了 5.55 dB，使所提取的纳

米结构信息更加可靠。测试并分析了不同曝光时间下所提方法的宇宙线去除性能，证明该方法能在长曝光积累场景下带来最佳的信噪比增益。该方法为周期性纳米结构的SAXS测量中宇宙线噪声的去除提供了可靠方案，提升SAXS测量图样的探测信噪比，进而提升SAXS的在线测量性能，具有重要的实际应用价值。

参 考 文 献

[1] Röntgen W C. On a new kind of rays[J]. Science, 1896, 3(59): 227-231.

[2] Miao J W, Chapman H N, Kirz J, et al. Taking X-ray diffraction to the limit: macromolecular structures from femtosecond X-ray pulses and diffraction microscopy of cells with synchrotron radiation[J]. Annual Review of Biophysics and Biomolecular Structure, 2004, 33: 157-176.

[3] 陶芬, 张玲, 苏博, 等. 上海同步辐射光源纳米三维成像线站设计、研发及调试[J]. 光学学报, 2022, 42(23): 2334001.
Tao F, Zhang L, Su B, et al. Design, development and commissioning of 3D nano image beamline at Shanghai synchrotron radiation facility[J]. Acta Optica Sinica, 2022, 42(23): 2334001.

[4] 杨海瑞, 谈志杰, 喻虹, 等. 基于单幅散斑的X射线强度关联缺陷检测方法[J]. 光学学报, 2023, 43(10): 1034001.
Yang H R, Tan Z J, Yu H, et al. X-ray intensity correlation defect detection using a single speckle pattern[J]. Acta Optica Sinica, 2023, 43(10): 1034001.

[5] 李卓越, 汪诚, 李秋良, 等. 基于X射线荧光和极端梯度提升的渗铝层厚度预测模型[J]. 激光与光电子学进展, 2022, 59(21): 2134001.
Li Z Y, Wang C, Li Q L, et al. Prediction model of aluminized layer thickness based on X-ray fluorescence and extreme gradient boosting[J]. Laser & Optoelectronics Progress, 2022, 59(21): 2134001.

[6] Lee J W, Park W B, Lee J H, et al. A deep-learning technique for phase identification in multiphase inorganic compounds using synthetic XRD powder patterns[J]. Nature Communications, 2020, 11(1): 86.

[7] 郭琦, 姜红, 杨金颉, 等. X射线荧光光谱结合深度学习算法可视化检验食品包装纸[J]. 激光与光电子学进展, 2022, 59(4): 0434001.
Guo Q, Jiang H, Yang J J, et al. Visual inspection of food packaging paper by X-ray fluorescence spectroscopy combined with deep learning algorithm[J]. Laser & Optoelectronics Progress, 2022, 59(4): 0434001.

[8] 宋海声, 陈召, 徐大诚, 等. GA-BP神经网络结合EDXRF技术实现对中低合金钢中Cr、Mn和Ni元素含量的预测[J]. 激光与光电子学进展, 2022, 59(12): 1234001.
Song H S, Chen Z, Xu D C, et al. Prediction of Cr, Mn, and Ni in medium and low alloy steels by GA-BP neural network combined with EDXRF technology[J]. Laser & Optoelectronics Progress, 2022, 59(12): 1234001.

[9] 程松, 杨洪刚, 徐学谦, 等. 基于YOLOv5的改进轻量型X射线铝合金焊缝缺陷检测算法[J]. 中国激光, 2022, 49(21): 2104005.
Cheng S, Yang H G, Xu X Q, et al. Improved lightweight X-ray aluminum alloy weld defects detection algorithm based on YOLOv5[J]. Chinese Journal of Lasers, 2022, 49(21): 2104005.

[10] Guinier A. La diffraction des rayons X aux très petits angles: application à l'étude de phénomènes ultramicroscopiques[J]. Annales De Physique, 1939, 11(12): 161-237.

[11] Debye P, Bueche A M. Scattering by an inhomogeneous solid [J]. Journal of Applied Physics, 1949, 20(6): 518-525.

[12] Porod G. Die röntgenkleinwinkelstreuung von dichtgepackten kolloiden systemen[J]. Kolloid-Zeitschrift, 1951, 124(2): 83-114.

[13] Hosemann R. Die parakristalline feinstruktur natürlicher und synthetischer eiweisse. Visuelles Näherungsverfahren zur bestimmung der schwankungstensoren von gitterzellen[J]. Acta Crystallographica, 1951, 4(6): 520-530.

[14] Wilkins M H, Blaurock A E, Engelman D M. Bilayer structure in membranes[J]. Nature: New Biology, 1971, 230(11): 72-76.

[15] Engelman D M. Lipid bilayer structure in the membrane of Mycoplasma laidlawii[J]. Journal of Molecular Biology, 1971, 58(1): 153-165.

[16] Perret R, Ruland W. Single and multiple X-ray small-angle scattering of carbon fibres[J]. Journal of Applied Crystallography, 1969, 2(5): 209-218.

[17] Fleury B, Cortes-Huerto R, Taché O, et al. Gold nanoparticle internal structure and symmetry probed by unified small-angle X-ray scattering and X-ray diffraction coupled with molecular dynamics analysis[J]. Nano Letters, 2015, 15(9): 6088-6094.

[18] Wu W L, Lin E K, Lin Q H, et al. Small angle neutron scattering measurements of nanoscale lithographic features[J]. Journal of Applied Physics, 2000, 88(12): 7298-7303.

[19] 陈修国, 王才, 杨天娟, 等. 集成电路制造在线光学测量检测技术：现状、挑战与发展趋势[J]. 激光与光电子学进展, 2022, 59(9): 0922025.
Chen X G, Wang C, Yang T J, et al. Inline optical measurement and inspection for IC manufacturing: state-of-the-art, challenges, and perspectives[J]. Laser & Optoelectronics Progress, 2022, 59(9): 0922025.

[20] Wormington M, Ginsburg A, Reichental I, et al. X-ray critical dimension metrology solution for high aspect ratio semiconductor structures[J]. Proceedings of SPIE, 2021, 11611: 116110W.

[21] Wu W L, Joseph Kline R, Jones R L, et al. Review of the key milestones in the development of critical dimension small angle X-ray scattering at National Institute of Standards and Technology [J]. Journal of Micro/Nanopatterning, Materials, and Metrology, 2023, 22(3): 031206.

[22] Kline R J, Sunday D F, Windover D, et al. X-ray scattering critical dimensional metrology using a compact X-ray source for next generation semiconductor devices[J]. Journal of Micro/Nanolithography, MEMS, and MOEMS, 2017, 16(1): 014001.

[23] Shanks T, Georgantopoulos I, Stewart G C, et al. The origin of the cosmic X-ray background[J]. Nature, 1991, 353: 315-320.

[24] Shaw R A, Horne K. Noise model-based cosmic ray rejection for WF/PC patterns[EB/OL]. [2023-11-09]. https://www.aspbooks.org/publications/25/311.pdf.

[25] van Dokkum P. Cosmic-ray rejection by Laplacian edge detection [J]. Publications of the Astronomical Society of the Pacific, 2001, 113(789): 1420-1427.

[26] Shamir L. A fuzzy logic-based algorithm for cosmic-ray hit rejection from single images[J]. Astronomische Nachrichten, 2005, 326(6): 428-431.

[27] Gin P, Wormington M, Amasay Y, et al. Inline metrology of high aspect ratio hole tilt and center line shift using small-angle X-ray scattering[J]. Journal of Micro/Nanopatterning, Materials, and Metrology, 2023, 22(3): 031205.

[28] Ito Y, Goto T, Suenaga R, et al. Characterization of deep-hole structure of semiconductor devices using transmission small-angle X-ray scattering[J]. Japanese Journal of Applied Physics, 2023, 62(4): 046501.

[29] Als-Nielsen J, McMorrow D. Elements of modern X-ray physics [M]. Weinheim: Wiley, 2011.

[30] 李贞杰, 张杰, 李木槿, 等. X射线像素探测器研究进展[J]. 科学通报, 2022, 67(32): 3808-3822.
Li Z J, Zhang J, Li M J, et al. Research advances on X-ray pixel detectors[J]. Chinese Science Bulletin, 2022, 67(32): 3808-3822.

[31] Kittel C. Introduction to solid state physics[M]. 8th ed.

Weinheim: John Wiley & Sons, 2018.
[32] Bonaque-González S. Cosmic-rays-generator[EB/OL]. [2023-12-11]. https://www.researchgate.net/publication/327155865_Cosmic-Rays-Generator.
[33] Tharwat A. Classification assessment methods[J]. Applied Computing and Informatics, 2021, 17(1): 168-192.
[34] Horé A, Ziou D. Image quality metrics: PSNR vs. SSIM[C]// 2010 20th International Conference on Pattern Recognition, August 23-26, 2010, Istanbul, Turkey. New York: IEEE Press, 2010: 2366-2369.

Cosmic Ray Rejection in Small Angle X-Ray Scattering

Zhao Jin[1,3], Wang Chenglong[2*], Yu Hong[1,2,3]

[1]*Key Laboratory for Quantum Optics, Shanghai Institute of Optics and Fine Mechanics, Chinese Academy of Sciences, Shanghai* 201800, *China*;
[2]*Zhangjiang Laboratory, Shanghai* 201210, *China*;
[3]*University of Chinese Academy of Sciences, Beijing* 100049, *China*

Abstract

Objective Small angle X-ray scattering (SAXS) is a powerful tool to measure structural features on the order of 1–100 nm. Due to high measurement accuracy and strong penetrability, SAXS attracts much attention to characterizing the complex three-dimensional (3D) structure information of periodic nanostructures in integrated circuit (IC) and has been successfully applied to high aspect ratio (HAR) structures, such as 3D-NAND and DRAM. SAXS for IC inline metrology is mostly based on compact X-ray sources. Limited by the brightness of compact X-ray sources, SAXS measurement requires a long exposure time to improve the signal-to-noise (SNR) of SAXS signals. Since the integration effect of long exposure time, numerous cosmic rays are inevitably introduced in the SAXS measurement pattern. As a typical kind of noise that is not correlated with SAXS signals, cosmic rays appear in SAXS patterns randomly and cause signal distortion, which has a negative effect on nanostructure information extraction. However, for lack of making full use of the signal's periodicity information, present cosmic ray rejection algorithms cannot accurately identify and remove the cosmic rays that have a real influence on SAXS signals in the measurement pattern. A new cosmic ray rejection method is needed for SAXS measurement patterns of periodic nanostructures, which will help improve the SNR of SAXS patterns and the performance of nanostructure information extraction.

Methods We propose a cosmic ray rejection method for the SAXS measurement pattern of periodic nanostructure. First, a pattern sequence including many short exposure SAXS measurement patterns of periodic nanostructure samples is generated in the same measurement conditions. Then, the coordinates of the periodic scattering signals are calculated by taking the periodic information of the nanostructure as physical prior, and cosmic rays existing in the effective signal area for each diffraction order in each scattering pattern are identified. After removing the abnormal frames influenced by cosmic rays from the pattern sequence, the SAXS measurement pattern after cosmic ray rejection is obtained by summing the remaining frames of the pattern sequence. The pattern sequence including 500 short exposure SAXS measurement patterns of periodic nanostructure samples is used to evaluate the performance of the proposed method. The precision, miss rate, and false alarm rate of cosmic ray detection results of the pattern sequence are calculated. Meanwhile, two existing methods for cosmic ray rejection of Laplacian edge detection and multi-frame median pixel rejection are selected as the comparison method, and the SAXS measurement pattern sequence is removed from cosmic rays by adopting the two comparison methods and the proposed method. The mean square error (MSE), peak signal-to-noise ratio (PSNR), and structural similarity (SSIM) of the pattern sequence before and after cosmic ray rejection by three methods are calculated respectively. Since the influence of cosmic rays and Poisson noise on the SAXS measurement pattern is relative to the exposure time, the competitive relationships between two kinds of noise and cosmic ray rejection performances of the proposed method in different exposure times are analyzed. This is realized by calculating the relationship of PSNR of the pattern sequence before and after denoising by three methods respectively, and the number of frames included in the sequence.

Results and Discussions According to the confusion matrix calculated based on the cosmic ray detection results of the pattern sequence including 500 short exposure SAXS measurement patterns (Fig. 4), the precision, miss rate, and false alarm rate are 87.67%, 4.93%, and 5.18%, respectively. Compared with the two comparison methods, the pattern

sequence denoised by this method has the best cosmic ray rejection effect, and the MSE, PSNR, and SSIM of the method are all optimal (Fig. 5 and Table 1). Especially, PSNR of the pattern sequence increases by 5.55 dB after removing cosmic rays by this method. When the number of frames included in the pattern sequence is low and equivalent to exposure time, Poisson noise is dominant and the PSNR of the pattern sequence is so low that we need more exposure time. When the number of frames increases to about 200, cosmic rays seriously restrict the upper limit of the PSNR of the scattering pattern. However, the PSNR of the pattern sequence after denoising by this method still increases with the rising number of frames, and the growth rate of the PSNR is significantly higher than comparison methods (Fig. 6).

Conclusions We propose a method for cosmic ray rejection in the SAXS measurement pattern of periodic nanostructures. The pattern sequence including 500 short exposure SAXS measurement patterns of periodic nanostructure samples is simulated and removed from cosmic rays by this method. According to the cosmic ray detection results, the miss rate and false alarm rate are both only about 5%, which proves that the proposed method has a sound detection effect on cosmic rays for the single frame scattering pattern. Meanwhile, the PSNR of the pattern sequence increases by 5.55 dB after removing cosmic rays by the proposed method. The PSNR gain greatly improves the extraction reliability and accuracy of the periodic nanostructure information. By analyzing the competitive relationship between Poisson noise and cosmic rays and evaluating the cosmic ray rejection performance of the proposed method in different exposure time, we find that this method can break the upper limit of PSNR caused by cosmic rays and improve PSNR of scattering pattern continuously. This proves that this method can obtain excellent PSNR gain in the long exposure integration condition. In principle, the proposed method provides a reliable cosmic ray rejection scheme for SAXS measurement patterns of periodic nanostructures, improving the detection SNR of SAXS patterns effectively. This method features a simple principle and fast operation and thus has practical significance to improve the inline metrology performance of SAXS.

Key words X-ray optics; small angle X-ray scattering; periodic nanostructure; cosmic ray; denoising